

Scalable wide-field optical coherence tomography-based angiography for in vivo imaging applications

Jingjiang Xu, Wei Wei, Shaozhen Song, Xiaoli Qi, and Ruikang K. Wang*

University of Washington, Department of Bioengineering, Seattle, Washington 98195, USA

*wangrk@uw.edu

Abstract: Recent advances in optical coherence tomography (OCT)-based angiography have demonstrated a variety of biomedical applications in the diagnosis and therapeutic monitoring of diseases with vascular involvement. While promising, its imaging field of view (FOV) is however still limited (typically less than 9 mm^2), which somehow slows down its clinical acceptance. In this paper, we report a high-speed spectral-domain OCT operating at 1310 nm to enable wide FOV up to 750 mm^2 . Using optical microangiography (OMAG) algorithm, we are able to map vascular networks within living biological tissues. Thanks to 2,048 pixel-array line scan InGaAs camera operating at 147 kHz scan rate, the system delivers a ranging depth of $\sim 7.5\text{ mm}$ and provides wide-field OCT-based angiography at a single data acquisition. We implement two imaging modes (i.e., wide-field mode and high-resolution mode) in the OCT system, which gives highly scalable FOV with flexible lateral resolution. We demonstrate scalable wide-field vascular imaging for multiple finger nail beds in human and whole brain in mice with skull left intact at a single 3D scan, promising new opportunities for wide-field OCT-based angiography for many clinical applications.

©2016 Optical Society of America

OCIS codes: (110.4500) Optical coherence tomography; (170.3880) Medical and biological imaging; (170.2655) Functional monitoring and imaging.

References and links

1. D. M. McDonald and P. L. Choyke, "Imaging of angiogenesis: from microscope to clinic," *Nat. Med.* **9**(6), 713–725 (2003).
2. E. B. Brown, R. B. Campbell, Y. Tsuzuki, L. Xu, P. Carmeliet, D. Fukumura, and R. K. Jain, "In vivo measurement of gene expression, angiogenesis and physiological function in tumors using multiphoton laser scanning microscopy," *Nat. Med.* **7**(7), 864–868 (2001).
3. M. A. Konerding, A. J. Miodonski, and A. Lametschwandner, "Microvascular corrosion casting in the study of tumor vascularity: a review," *Scanning Microsc.* **9**(4), 1233–1244 (1995).
4. H. Hashizume, P. Baluk, S. Morikawa, J. W. McLean, G. Thurston, S. Roberge, R. K. Jain, and D. M. McDonald, "Openings between defective endothelial cells explain tumor vessel leakiness," *Am. J. Pathol.* **156**(4), 1363–1380 (2000).
5. R. Weissleder, "Scaling down imaging: Molecular mapping of cancer in mice," *Nat. Rev. Cancer* **2**(1), 11–18 (2002).
6. J. D. Pearlman, R. J. Laham, M. Post, T. Leiner, and M. Simons, "Medical imaging techniques in the evaluation of strategies for therapeutic angiogenesis," *Curr. Pharm. Des.* **8**(16), 1467–1496 (2002).
7. W. Drexler and J. G. Fujimoto, "Optical Coherence Tomography: Technology and Applications (Biological and Medical Physics, Biomedical Engineering)," Springer (2008).
8. W. Drexler, "Ultrahigh-resolution optical coherence tomography," *J. Biomed. Opt.* **9**(1), 47–74 (2004).
9. J. Xu, X. Wei, L. Yu, C. Zhang, J. Xu, K. K. Wong, and K. K. Tsia, "High-performance multi-megahertz optical coherence tomography based on amplified optical time-stretch," *Biomed. Opt. Express* **6**(4), 1340–1350 (2015).
10. I. Grulkowski, J. J. Liu, B. Potsaid, V. Jayaraman, J. Jiang, J. G. Fujimoto, and A. E. Cable, "High-precision, high-accuracy ultralong-range swept-source optical coherence tomography using vertical cavity surface emitting laser light source," *Opt. Lett.* **38**(5), 673–675 (2013).

11. R. K. K. Wang, X. Q. Xu, V. V. Tuchin, and J. B. Elder, "Concurrent enhancement of imaging depth and contrast for optical coherence tomography by hyperosmotic agents," *J. Opt. Soc. Am. B* **18**(7), 948–953 (2001).
12. V. V. Tuchin, X. Xu, and R. K. Wang, "Dynamic optical coherence tomography in studies of optical clearing, sedimentation, and aggregation of immersed blood," *Appl. Opt.* **41**(1), 258–271 (2002).
13. H. Wang and A. M. Rollins, "Speckle reduction in optical coherence tomography using angular compounding by B-scan Doppler-shift encoding," *J. Biomed. Opt.* **14**(3), 030512 (2009).
14. N. Ifimian, B. E. Bouma, and G. J. Tearney, "Speckle reduction in optical coherence tomography by "path length encoded" angular compounding," *J. Biomed. Opt.* **8**(2), 260–263 (2003).
15. M. Pircher, E. Gotzinger, R. Leitgeb, A. F. Fercher, and C. K. Hitzenberger, "Speckle reduction in optical coherence tomography by frequency compounding," *J. Biomed. Opt.* **8**(3), 565–569 (2003).
16. B. Hermann, E. J. Fernández, A. Unterhuber, H. Sattmann, A. F. Fercher, W. Drexler, P. M. Prieto, and P. Artal, "Adaptive-optics ultrahigh-resolution optical coherence tomography," *Opt. Lett.* **29**(18), 2142–2144 (2004).
17. J. Jang, J. Lim, H. Yu, H. Choi, J. Ha, J. H. Park, W. Y. Oh, W. Jang, S. Lee, and Y. Park, "Complex wavefront shaping for optimal depth-selective focusing in optical coherence tomography," *Opt. Express* **21**(3), 2890–2902 (2013).
18. R. K. Wang, S. L. Jacques, Z. Ma, S. Hurst, S. R. Hanson, and A. Gruber, "Three dimensional optical angiography," *Opt. Express* **15**(7), 4083–4097 (2007).
19. A. Mariampillai, B. A. Standish, E. H. Moriyama, M. Khurana, N. R. Munce, M. K. K. Leung, J. Jiang, A. Cable, B. C. Wilson, I. A. Vitkin, and V. X. D. Yang, "Speckle variance detection of microvasculature using swept-source optical coherence tomography," *Opt. Lett.* **33**(13), 1530–1532 (2008).
20. M. S. Mahmud, D. W. Cadotte, B. Vuong, C. Sun, T. W. H. Luk, A. Mariampillai, and V. X. D. Yang, "Review of speckle and phase variance optical coherence tomography to visualize microvascular networks," *J. Biomed. Opt.* **18**(5), 050901 (2013).
21. L. An, J. Qin, and R. K. Wang, "Ultrahigh sensitive optical microangiography for in vivo imaging of microcirculations within human skin tissue beds," *Opt. Express* **18**(8), 8220–8228 (2010).
22. R. K. Wang, L. An, P. Francis, and D. J. Wilson, "Depth-resolved imaging of capillary networks in retina and choroid using ultrahigh sensitive optical microangiography," *Opt. Lett.* **35**(9), 1467–1469 (2010).
23. Y. Jia, L. An, and R. K. K. Wang, "Label-free and highly sensitive optical imaging of detailed microcirculation within meninges and cortex in mice with the cranium left intact," *J. Biomed. Opt.* **15**(3), 030510 (2010).
24. Q. Zhang, Y. Huang, T. Zhang, S. Kubach, L. An, M. Laron, U. Sharma, and R. K. K. Wang, "Wide-field imaging of retinal vasculature using optical coherence tomography-based microangiography provided by motion tracking," *J. Biomed. Opt.* **20**(6), 066008 (2015).
25. J. P. Kolb, T. Klein, C. L. Kufner, W. Wieser, A. S. Neubauer, and R. Huber, "Ultra-widefield retinal MHz-OCT imaging with up to 100 degrees viewing angle," *Biomed. Opt. Express* **6**(5), 1534–1552 (2015).
26. H. Wang, U. Baran, and R. K. Wang, "In vivo blood flow imaging of inflammatory human skin induced by tape stripping using optical microangiography," *J. Biophotonics* **8**(3), 265–272 (2015).
27. U. Baran, L. Shi, and R. K. Wang, "Capillary blood flow imaging within human finger cuticle using optical microangiography," *J. Biophotonics* **8**(1-2), 46–51 (2015).
28. Y. Li, U. Baran, and R. K. K. Wang, "Application of Thinned-Skull Cranial Window to Mouse Cerebral Blood Flow Imaging Using Optical Microangiography," *PLoS One* **9**(11), e113658 (2014).
29. S. Clark, F. Campbell, T. Moore, M. I. Jayson, T. A. King, and A. L. Herrick, "Laser Doppler imaging—a new technique for quantifying microcirculatory flow in patients with primary Raynaud's phenomenon and systemic sclerosis," *Microvasc. Res.* **57**(3), 284–291 (1999).
30. S. M. S. Kazmi, A. B. Parthasarthy, N. E. Song, T. A. Jones, and A. K. Dunn, "Chronic imaging of cortical blood flow using Multi-Exposure Speckle Imaging," *J. Cereb. Blood Flow Metab.* **33**(6), 798–808 (2013).
31. J. Yao and L. V. Wang, "Photoacoustic brain imaging: from microscopic to macroscopic scales," *Neurophotonics* **1**(1), 011003 (2014).
32. H. Zafar, J. Enfield, M. L. O'Connell, B. Ramsay, M. Lynch, and M. J. Leahy, "Assessment of psoriatic plaque in vivo with correlation mapping optical coherence tomography," *Skin Res. Technol.* **20**(2), 141–146 (2014).
33. S. Yousefi, Z. W. Zhi, and R. K. K. Wang, "Eigendecomposition-Based Clutter Filtering Technique for Optical Microangiography," *IEEE Trans. Biomed. Eng.* **58**(8), 2316–2323 (2011).
34. P. H. Tomlins and R. Wang, "Theory, developments and applications of optical coherence tomography," *J. Phys. D Appl. Phys.* **38**(15), 2519–2535 (2005).
35. R. S. Fawcett, S. Linford, and D. L. Stulberg, "Nail abnormalities: clues to systemic disease," *Am. Fam. Physician* **69**(6), 1417–1424 (2004).
36. M. Williams, "Examining the fingernails when evaluating presenting symptoms in elderly patients," Retrieved March 20, 2011 (2009).
37. A. Zhang, Q. Zhang, and R. K. Wang, "Minimizing projection artifacts for accurate presentation of choroidal neovascularization in OCT micro-angiography," *Biomed. Opt. Express* **6**(10), 4130–4143 (2015).
38. W. Wieser, B. R. Biedermann, T. Klein, C. M. Eigenwillig, and R. Huber, "Multi-Megahertz OCT: High quality 3D imaging at 20 million A-scans and 4.5 GVoxels per second," *Opt. Express* **18**(14), 14685–14704 (2010).
39. J. Xu, C. Zhang, J. Xu, K. K. Wong, and K. K. Tsia, "Megahertz all-optical swept-source optical coherence tomography based on broadband amplified optical time-stretch," *Opt. Lett.* **39**(3), 622–625 (2014).

1. Introduction

The visualization of functional vascular networks and architecture of blood vessels within living biological tissue plays a critical role in the diagnosis and therapeutic monitoring of diseases, as well as in the study of tissue pathology and morphology [1]. So far, a variety of imaging technologies have been developed for visualizing vascular beds in animal models or in humans at different scales. At microscopic scale, the imaging modalities, e.g., confocal, multiphoton and fluorescence microscopy and scanning electron microscopic imaging, allow for cellular structural and functional visualization to elucidate abnormalities of vessel angiogenesis and remodeling [2–4]. Although these microscopy-based imaging methods are capable of achieving superior spatial resolution, ranging from a few nanometers to sub-microns, the shallow imaging depth and small field of view (FOV) often limit their applications to small specimens or preserved samples that require laborious tissue biopsy and preparation. At macroscopic scale, X-ray computed tomography, positron emission tomography, ultrasound imaging and magnetic resonance imaging have been well utilized for clinical applications to provide angiogenesis assessment in deep tissues within the whole body of animals and humans [5, 6]. However, the spatial resolution of these techniques typically ranges from a few hundreds of microns to a few millimeters or more in standard clinical practice. The coarse-grained resolution is unable to provide the detailed examination of blood microcirculation within tissue. The dilemma between the microscopic and macroscopic methods necessitates the development of imaging modalities that can bridge the gap of resolution and penetration. Among numerous imaging methods, optical coherence tomography (OCT) is one of the most promising alternatives to fill this gap because OCT is capable of providing micron-level spatial resolution with reasonable imaging depth in tissue.

Over decades of developments in optics, detection, fibers as well as laser technology, OCT has become an indispensable tool in biomedical imaging due to its capability of real-time, three-dimensional (3D), label-free and high-sensitive visualization of intact tissue and specimens [7]. Largely due to the performance of light source (mainly the wavelength and spectral bandwidth), OCT can achieve micron-scale axial resolution ($<10\ \mu\text{m}$), providing high-precision in-depth images for subcellular biometry *in vivo* [8]. Another important attribute of the OCT technology is its highly scalable imaging depth, i.e., depth ranging. The depth ranging of the most common commercial OCT system is typically from 2 to 4 mm, which is sufficient for most retinal and endoscopic imaging applications. With recent advances in light source and detection technology, the OCT depth ranging has been improved from multi-centimeters up to a few meters, promising new opportunities for biomedical applications, such as the bulk imaging of entire anterior segment, full eye length, or upper airway in human body, accomplished by one 3D scan [9, 10]. Moreover, the techniques of optical clearing [11, 12], spatial and frequency compounding [13–15] as well as wavefront correction [16, 17], are reported to reduce multiple scattering effect in biological samples so that the imaging depth is increased, which are significant for intravascular or intraluminal imaging in deep tissues. As an important extensions of traditional OCT technique, optical angiography or optical microangiography (OMAG) has been utilized to construct functional 3D vascular networks or blood perfusion maps by measuring the changes in amplitude, phase and complex value of the OCT signals [18–20]. Recently, ultra-high sensitive OMAG has been reported to achieve unprecedented flow sensitivity down to capillary level where flow velocity is often slow, ranging from $\sim 10\ \mu\text{m/s}$ to $\sim 100\ \mu\text{m/s}$ [21]. The OMAG method has been successfully used for vascular imaging of microcirculation within human skin [21], retina and choroid [22], and mouse brain [23]. However, most of these OMAG systems suffer from small area of picturing (typically a few mm^2), thus requiring defined scan region for imaging that is unfortunately often not known *a priori*. In many clinical applications, it is usually required to assess vascular tissue beds covering a large field of view ($>100\ \text{mm}^2$) at a glance so that the region of interests, or diseased regions can be quickly identified for further

detailed examination. To achieve wide field imaging, multiple cube scanning strategy, i.e. montaging scanning method [24], is reported. While promising, this montaging approach is however time consuming, leading to a long scan time to obtain the final montaged results, which may affect the patient compliance for imaging. Therefore, wide-field OCT-based angiography at single 3D acquisition is desirable for clinical translation.

An impressive work of Kolb *et al* has demonstrated a high-speed ultra-wide-field OCT retinal imaging up to 100 degrees viewing angle, showing great potential for peripheral retinal visualization to aid ophthalmic diagnosis [25]. Apart from ophthalmology, there is also an increasing need and vivid interest of wide-field OCT-based angiography in the fields, such as dermatology, neurology, oncology, cardiology and endoscopy. For example, the abnormal microcirculation of finger nail-fold area is a significant sign of serious illness, such as anemia, liver disease, thyroid disease and malnutrition, which is possible to appear at any location over a large area of finger nail-fold. However, due to the performances of most current OCT systems, i.e., relatively slow A-scan rate, short depth ranging distance, and poor penetration power, only a small portion of blood vessels in the dorsal nail-fold area and finger cuticle were demonstrated in previous works [26, 27]. In addition, the volumetric imaging of cerebrovascular networks of the whole brain in mouse is critical to improve our fundamental understanding of the underlying mechanisms in neurological studies. However, most of current OCT systems requires open-skull cranial window or thinned-skull cranial window in a small region for OMAG imaging, which limits the assessment of the connection in the entire vascular system of mouse brain [28]. Although laser Doppler imaging (LDI) [29] and laser speckle imaging (LSI) [30] allows for *in vivo* evaluation of vascular abnormalities over a wide FOV, these methods are unable to provide detailed volumetric microvascular imaging. Photoacoustic microscopy (PAM) is also a powerful non-invasive imaging tool, which has been demonstrated for multi-scale vascular visualization to bridge the gap between microscopic and macroscopic imaging [31]. However, the contrast mechanisms is different between PAM and OCT, where PAM is mainly based on optical absorption of hemoglobin and melanin in blood vessel, while OMAG is an optical-scattering based imaging modality that provides both the structural morphology and vascular information of tissue in parallel. Moreover, considering the complexity and cost involved with PAM system, OMAG is a much more cost-effective and time-efficient imaging modality [32].

In this paper, we demonstrate a high-speed, high-sensitive functional OCT-based angiography system that can provide scalable FOV imaging, i.e. wide FOV imaging for quick assessment for diseased regions and small FOV imaging for detailed examination. Owing to the high-speed line scan InGaAs camera with 2048 pixel-array employed in the system, the imaging depth and data acquisition time has been greatly improved to meet the requirement for wide field of view imaging. Using the wide-field mode by employing a long focal-length lens in the sample arm, it can provide vascular mapping with unprecedented FOV. The high-resolution mode is enabled by switching the lens to a high-magnification objective lens, for detailed vascular imaging.

2. Experimental implementation

The experimental setup of the dual-mode OCT-based angiography system for scalable wide-field vascular imaging is shown in Fig. 1. In this setup, we used a broadband infrared superluminescent diode (SLD) centered at 1310 nm with an output power of ~13 mW as the OCT light source. The full width at half-maximum (FWHM) bandwidth of the SLD is ~60 nm, which provides ~13 μ m in air (~9 μ m in tissue). The light from the SLD was launched into fiber-based spectral-domain Michelson interferometer via a broadband optical circulator and then split into the reference arm and sample arm by a 50:50 fiber coupler (10202A-50, Thorlabs). In order to map the tissue into 3D structural and vascular optical images over a wide-field area, the probe beam in the sample arm was scanned by a pair of XY galvanometric mirrors (GVS002, Thorlabs). The power of the focused beam incident on the

sample was ~ 5 mW, which is below the American National Standards Institute (ANSI) standards during the measurement. In the sample arm, a turret mount was used to house two objective lens. One objective was a lens that has a long focal length of 75 mm, which was used to enable wide-field imaging mode for the system. The wide-field imaging serves as a navigation of quick visualization over a large FOV. Another objective was a $10\times$ magnification objective lens (LSM02, Thorlabs), giving high-resolution imaging mode for the system to provide a detailed examination of the sample (e.g. regions of interests). Currently, we used manual turning of the turret to switch between wide FOV and high-resolution modes. In order to accommodate the objective lens switching in the sample arm, a flipping mirror was implemented at the reference arm to quickly compensate the optical path length difference between the OCT arms when switching the imaging modes. Since the excursion of the galvo-mirror determines how wide the system scans, the driving voltage applied to galvanometric scanner is accordingly modified and pre-calibrated to provide precise FOV control in different imaging modes. Besides, as we employed different optical components in the two imaging modes, the dispersion mismatch between the reference arm and sample required to be compensated separately. This issue was met by separate system calibration to minimize the dispersion effect on the final results.

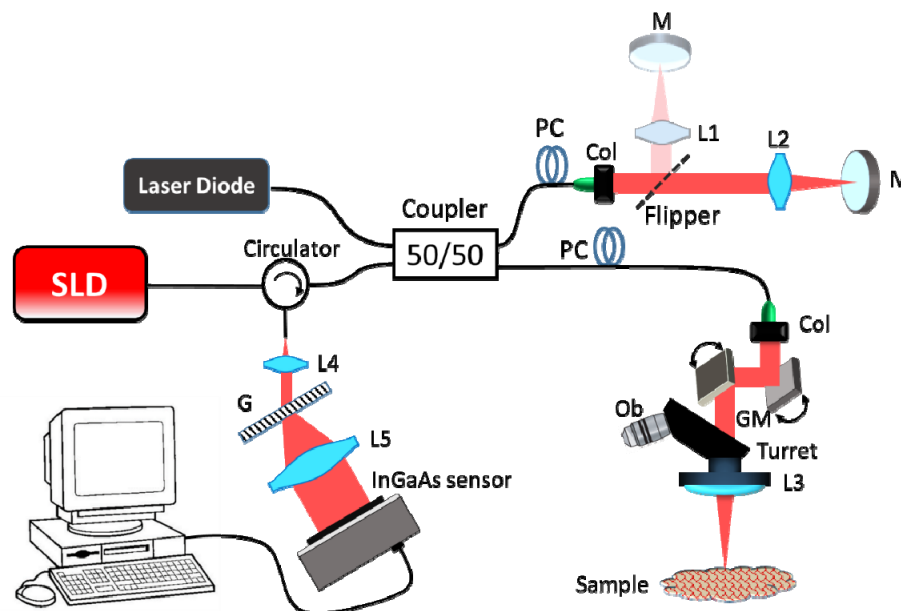


Fig. 1. Experimental setup of dual-mode OCT-based angiography system for scalable wide-field imaging. SLD: superluminescent diode, PC: polarization controller, Col: collimator, L1-L3: lenses of different specifications, M: mirror, GM: galvanometric mirrors, Ob: objective lens, G: grating.

The reflected lights from OCT arms were routed into a home-built spectrometer via the broadband optical circulator. This spectrometer was equipped with a high-performance InGaAs line scan camera with 2048 pixel-array (GL2048R, Sensors Ltd.) that allows for a maximum imaging speed of 147 kHz A-scan rate. The spectrometer had a designed spectral resolution of ~ 0.058 nm, providing ~ 7.5 mm ranging distance for the OCT system (See below). The spectral interferogram data sensed by the camera was transmitted to a host computer (Intel Xeon, 2.13GHz, 34 GB RAM) via a Camera Link® interface. In addition, a 635 nm visible laser diode (S1FC635PM, Thorlabs) was coupled into the system in order to guide the scanning position on the sample during imaging. The actions of line scan camera

initialization, galvo-scanning, data acquisition and storage were automatically controlled by a software package written in Labview language.

In order to enhance the final OCT-based angiography imaging quality, the OMAG scanning protocol was adopted [21]. The X-scanner (fast B-scan) was driven with a saw tooth waveform, which provided A-scans between 300 and 1000 per B frame depending on the step size requirement for different scanning protocols. And the Y-scanner (slow C-scan) was driven by a step function waveform, which also provided a variable number of locations (between 450 and 800 locations) with 5 repeated B frames per location. The duty cycle of the saw tooth waveform is set at ~85% of rising edge per cycle. Depending on how many A-scans are required for each B frame, the frame rate that can be afforded by the system was ranging from ~130 to 370 B-frames per second. The resulted different B-frame time intervals were still capable to provide high sensitive blood flow imaging in the OCT system. The parameters in the scanning protocol can be flexibly set at a user dialog-interface, written by Labview[®] language.

The repeated OCT measurement at each voxel is considered as the superposition of stationary signal (non-moving tissue structure), hemodynamic signal (mostly moving blood cells within patent vessels) and noise (shot noise and system noise). The data processing was done by employing Eigen-decomposition (ED)-based OMAG algorithm [33], which can effectively separate the static bulk tissue signal (e.g., non-moving tissue structural components) from dynamic scatter signals (e.g., flowing components in vascular networks) through synergistically utilizing both the amplitude and phase information of complex OCT signals. This ED-based clutter filtering algorithm enables the visualization of small vessels and capillaries as well as big vessels in various living tissues. At present, the captured data is processed off-line using MATLAB (MathWorks) platform.

3. Results

3.1 OCT system performance

To test the resolution performance of the proposed wide-field OCT-based angiography system, we first tested a U.S. Air Force test target (1951 USAF, Edmund Optics Inc.) in order to measure the lateral resolutions offered by the two imaging modes, i.e. wide and high-resolution FOV modes. The wide FOV mode provides a scan region that is larger than the USAF test chart, as shown in Fig. 2(a). This figure is given in a form of *en face* view, produced by maximum intensity projection (MIP) of the resolution target with a FOV of $23.3 \times 23.3 \text{ mm}^2$ and a spacing of $46.6 \text{ }\mu\text{m}$ between adjacent A-scans and B-scans. This FOV covers all the etching patterns. The ring-shaped fringes appearing in Fig. 2(a) were due to the interference created by the reflections between the surfaces of sample target and reference mirror. Also, the non-uniform brightness of the background in Fig. 2(a) was resulted from the different reflection efficiency over a large FOV caused by the aberration and distortion of the objective lens in wide-field mode. To measure the lateral resolution of the system in this wide FOV mode, we narrowed the scanning range to $1.8 \times 1.8 \text{ mm}^2$ with the spacing of $\sim 5 \text{ }\mu\text{m}$ between adjacent A-scans and B-scans, and captured a zoomed-in *en face* image of the resolution target (shown in Fig. 2(b)). A line intensity profile, at the right side in Fig. 2(b), of the *en face* image at the position indicated by the red dashed line shows the image contrast. The smallest pattern that can be resolved by the wide FOV mode is the element 3 in the group 4, as pointed by the red arrow, upon which the full width at half maximum (FWHM) contrast of the line width is measured at $24.8 \text{ }\mu\text{m}$. This can be regarded as the measured lateral resolution, which is agreed well with the calculated beam spot size of $23.6 \text{ }\mu\text{m}$ for the objective lens employed in this wide FOV mode.

For the high-resolution, small FOV imaging mode, an $10\times$ magnification objective lens (LSM02, Thorlabs) was employed, as described above. For resolution test, we elected to use a FOV of $0.5 \times 0.5 \text{ mm}^2$ with a spacing of $\sim 2 \text{ }\mu\text{m}$ between adjacent A-scans and B-scans.

According to the *en face* image of the resolution target and the line intensity profile of the green dashed line (shown in Fig. 2(c)) measured by the system, the element 4 in the group 6 with the line width of 5.52 μm can be resolved at the FWHM OCT signal contrast. Therefore, the lateral resolution of the high-resolution mode of the OCT system is determined to be $\sim 6 \mu\text{m}$. The small FOV with telecentric objective lens provides us a flat image plane, which leads to uniform brightness of background in Fig. 2(c). This high-resolution imaging mode is expected to give us the ability to visualize detailed blood perfusion of microcirculation at capillary level ($<10 \mu\text{m}$) within living tissue.

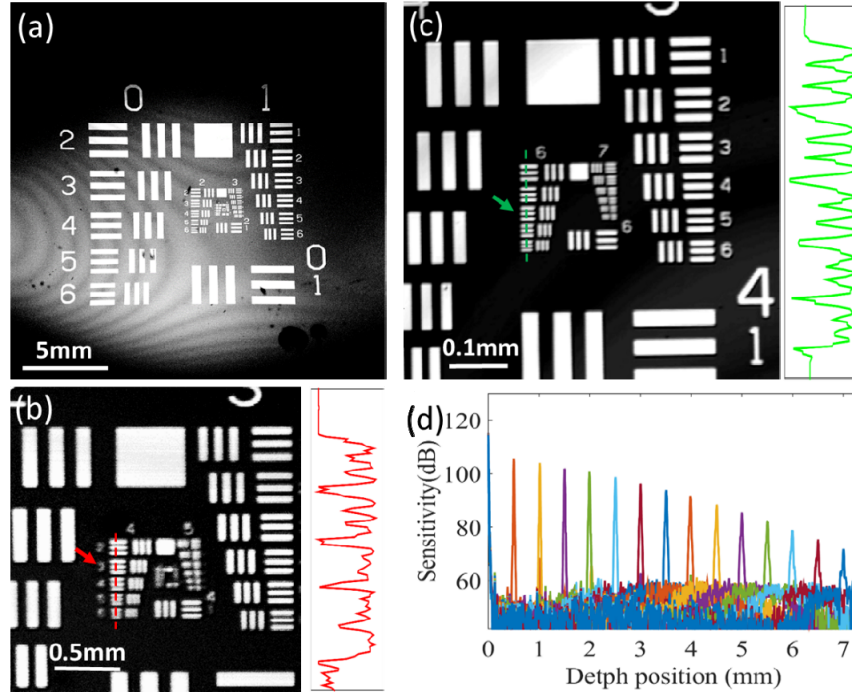


Fig. 2. Performance test of the proposed system using a 1951 USAF test target. (a), wide-field *en face* image of the test target and (b) the corresponding *en face* image using zoom-in scanning, along with a line intensity profile at the right side. (c) *en face* image of the test target produced by the high-resolution small FOV imaging mode, along with a line intensity profile at the right side. (d) System sensitivity roll-off measurement of the wide field OCT system.

Another important performance test of this OCT-based angiography system is the measurement of sensitivity roll-off characteristics for the assessment of the depth ranging. Due to surface unflatness for most bulk biological tissues, the depth ranging in the axial direction has a significant impact on the OCT images if scanned over a large FOV. The theoretical maximum depth ranging of a Fourier domain OCT system is defined by

$$z_{\max} = \frac{\lambda_0^2 N}{4n \cdot \Delta\lambda} \quad [34],$$

where N is the number of detecting elements. Most of the current

1310/1060 nm SD-OCT utilizes a line scan camera that has pixel numbers between 512 and 1024, which would often limit the effective ranging distance to 2~4 mm in air. Due to this limitation plus the characteristic sensitivity fall-off of the system, one often looks for a flat region of biological tissue for imaging, which is clearly not desirable for many practical applications. In our case, we employed a high-speed InGaAs line scan camera with 2048 pixel-array capable of 147 kHz A-scan rate, leading to a calculated maximum depth ranging of ~ 7.5 mm, relaxing the requirement of relatively flat region of tissue for imaging. Figure 2(d) shows the roll-off performance over a ranging distance of ~ 7.5 mm measured for the OCT

system. The OCT sensitivity is 105 dB measured at the depth position of 0.5 mm, and dropped to 81 dB at the depth position of 6 mm, indicating a roll-off number of ~ 0.23 mm/dB. As shown in the measurement, we are able to maintain a practically high sensitivity (> 80 dB) for vascular imaging over a long imaging distance (~ 6 mm). This long depth ranging is quite favorable in wide-field OCT system for biomedical imaging.

3.2 OCT/OMAG imaging of human fingers in vivo

To demonstrate the wide field imaging performances afforded by the proposed system, we conducted functional imaging of human fingers in volunteers *in vivo*. The preliminary study that uses home-built systems to image human subjects was reviewed and approved by Institutional Review Board of University of Washington, and the informed consent was obtained from all subjects before imaging. This study followed the tenets of the Declaration of Helsinki and was conducted in compliance with the Health Insurance Portability and Accountability Act.

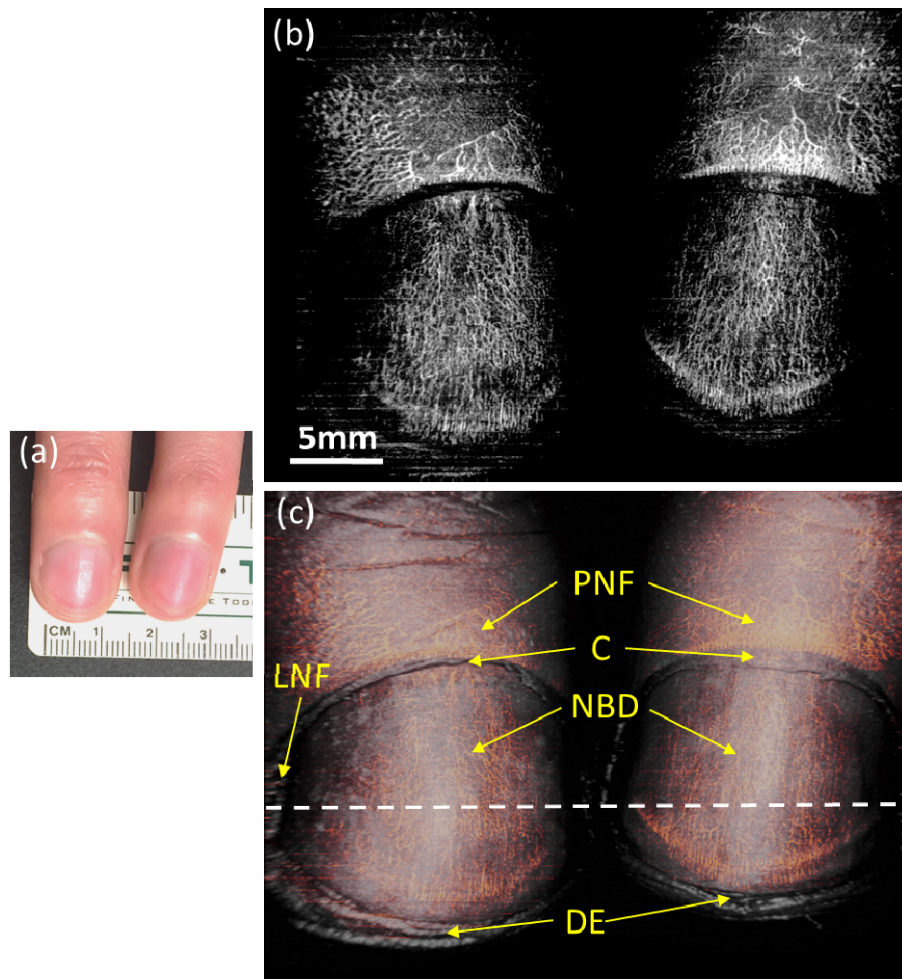


Fig. 3. Proposed OCT/OMAG system provides unprecedented FOV imaging of multiple fingers in one single 3D scan. (a) Photograph of the middle finger and ring finger with a ruler placed below. (b) The *en face* MIP vascular image of the two fingers with a 30×25 mm² FOV. (c) The corresponding 3D rendered structural image (grey color) overlaid with blood vascular networks (orange color). PNF: proximal nail fold, C: cuticle, NBD: nail body, DE: distal edge, LNF: lateral nail folds.

Figure 3(a) shows the photograph of the middle finger and ring finger on the left hand of a healthy male volunteer. As indicated by a standard metric ruler placed below the finger, the width of these two fingers is ~ 3 centimeters. It would present almost an impossible task if imaging is required to capture both fingers at one single scan using most conventional OCT systems. Figure 3(b) shows the OMAG *en face* image of the blood vessel networks within these two fingers using the wide FOV imaging mode of our proposed system. In this imaging, we set the field of view at $30 \times 25 \text{ mm}^2$ (fast- x slow-scan directions). We captured 1000 A lines per B frame with 800 locations along slow scanning direction, providing about $30 \mu\text{m}$ spacing between A-scans in both the fast and slow directions. Based on the speed of the line scan camera (147 kHz) and the duty cycle of the fast scanning (85%), we set the frame rate at 127 B-frame/s during imaging. The data acquisition was accomplished within ~ 31 s with 5 repeated B-scans per location. The motion artifacts shown in the vascular image is due to the slow B-frame rate and the long data acquisition time. Figure 3(c) shows the corresponding 3D rendered image of the two fingers, resulting from overlying the structural image (grey color) with the vascular image (orange color). In this figure, we are able to identify blood circulation within different regions, such as proximal nail fold, cuticle, nail body, distal edge and lateral nail folds at one glance. Figure 4 shows representative cross-section B-scans of both structural and blood flow images, obtained from a location marked by the white dashed line in Fig. 3(c) to indicate depth-resolved structural and vascular features within this wide field of view. This unprecedented FOV (750 mm^2) imaging, however, contains a large number of data points, making the data acquisition time as long as 31 sec.

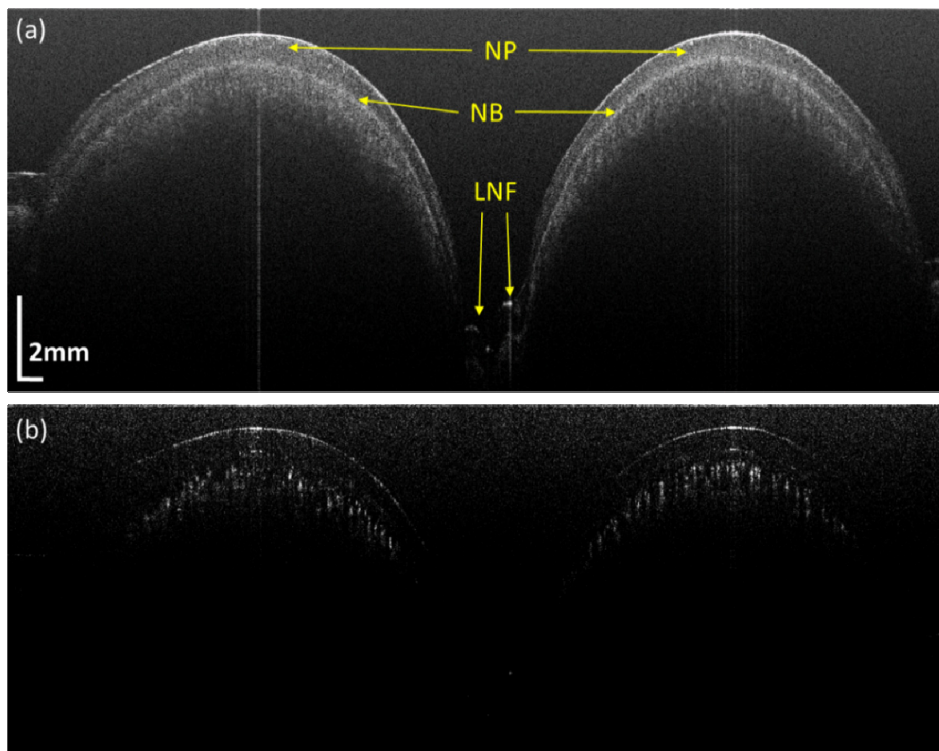


Fig. 4. (a) The structural image (a) and blood flow image (b) in nail fold as indicated by the white-dashed line in Fig. 3(c). NP: nail plate, NB: nail bed, LNF: lateral nail folds.

In order to reduce the scanning time for the benefit of volunteer's comfort, we decreased the FOV to $18 \times 18 \text{ mm}^2$ for imaging. Under this circumstance, the ring finger can be covered in one single scan. In doing so, we employed 500 A-scans and 500 locations with 5 repetitions

(shown in Fig. 5(a)-5(b)). Accordingly, a B-scan rate of 230 frame/s can be afforded due to the reduction of A-line numbers per B frame. Consequently, the data acquisition time for this zoomed-in image took ~11 s, which is more favorable for practical applications. Figure 5(c) shows the cross-sectional structural image at the position of proximal nail fold as indicated by the green dashed line in Fig. 5(b). In the structural image, it is obvious that the OCT can distinguish the anatomical layers of skin, nail plate and nail beds. Figure 5(d) is the corresponding OMAG blood flow image that shows a high density of blood vessels located between the superficial skin layer and the nail plate. The rich blood vessels around the cuticle region plays an important role to transport and maintain the nutrition in order to support the growth of the nail body. Figures 5(e) and 5(f) are the structural image and corresponding blood flow image at the region of nail body. Using the NIR light source together with a long focal-length lens at the sample arm, we were able to visualize the deep blood vessels beneath the thick layer of nail plate.

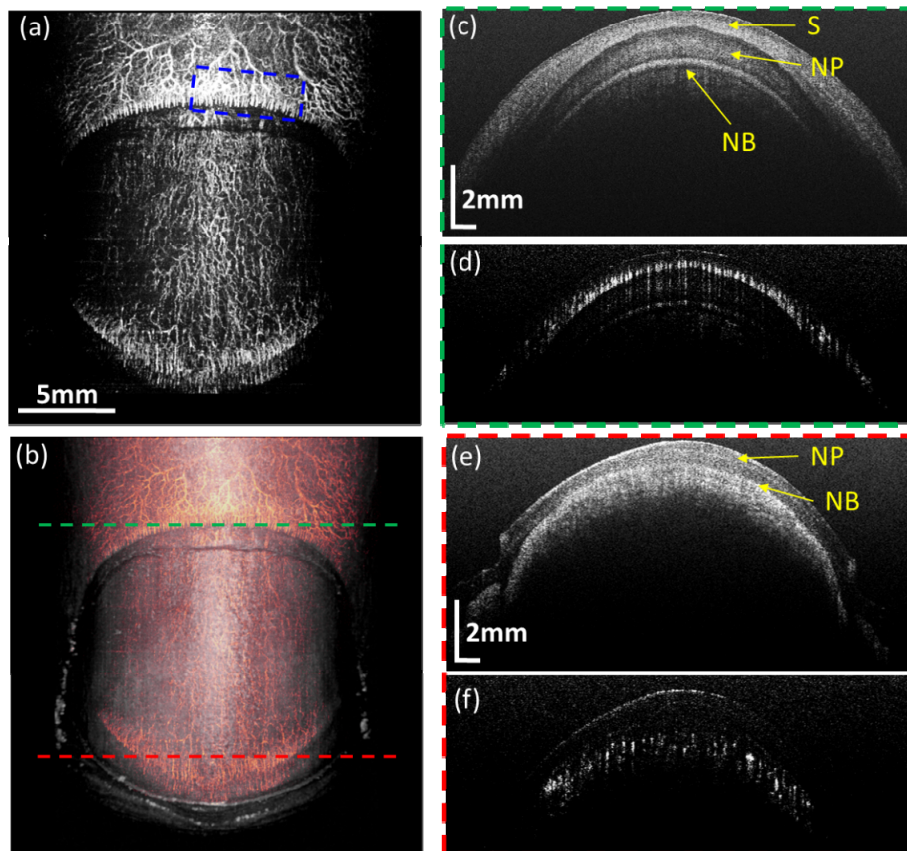


Fig. 5. Proposed system provides detailed visualization of anatomical features of both structure and blood flow within one whole signal in one scan. (a) The zoomed-in *en face* MIP vascular image of the ring fingers with $18 \times 18 \text{ mm}^2$ FOV. (b) The corresponding 3D rendered structural image (grey color) overlaid with blood vascular networks (orange color). The structural image (c) and blood flow image (d) are obtained from a position of proximal nail fold as indicated by the green dashed line in (b). The structural image (e) and blood flow image (f) are from nail fold beds as indicated by the red dashed line in (b). S: skin, NP: nail plate, NB: nail bed.

Since the tissue around the cuticle region contains characteristic structures that are richly perfused with blood, we investigated this region using high-resolution FOV mode, in which a $10 \times$ objective lens was employed, so that detailed information can be examined. For this, the

FOV was set at $3.0 \times 4.5 \text{ mm}^2$, containing 300 A-scans per B scan and 450 locations with 5 B-scan repetitions, which required $\sim 6 \text{ s}$ for data acquisition. The results scanned from the tissue region marked by a blue box in Fig. 5(a) are shown in Fig. 6. The high resolution mode enabled us to visualize the hair pin-like capillary loops in the human finger cuticle as shown in Fig. 6(a). Figures 6(c) and 6(d) are the representative cross-sectional structural image and corresponding blood flow image at the position marked by the green dashed line shown in Fig. 6(b). Figure 6(b) was obtained by overlying the volumetric blood flow image (orange color) with the structural image (grey scale). The detailed layer structures of epidermis, dermis, nail matrix, nail root and nail beds are clearly differentiated in Fig. 6(c). The blood vessels are mainly distributed within the layer of dermis (Fig. 6(d)). Due to the fast B-scan rate and short data acquisition time, the motion artifacts in the small FOV vascular images are less severe, which give the image with relatively high contrast. With this scalable wide-field OCT system that is capable of providing not only the structural but also the vascular information, it may be clinically useful to aid the examination of the health conditions of the nail fold beds in human fingers from macroscopic scale to microscopic scale within a time frame of seconds. Thus, it could promise to serve as a potential non-invasive and versatile imaging tool for screening the nail-fold related diseases, such as fungal infection, psoriasis, malnutrition, inflammatory arthritis, anemia and thyroid dysfunction, to name just a few [35, 36].

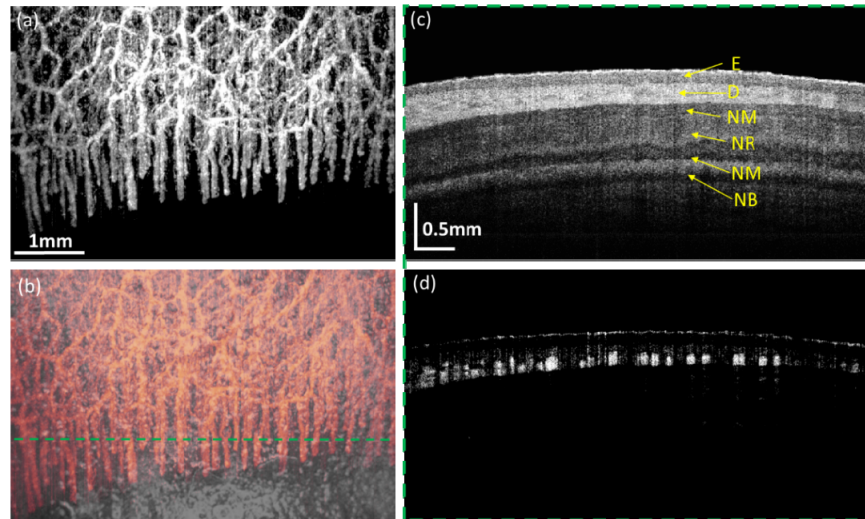


Fig. 6. High resolution mode of the system provides detailed visualization of tissue structures and vessel networks including capillary vessels. (a) The *en face* MIP vascular image at the junction area (blue dashed box in Fig. 4(a)) of the ring fingers with a FOV of $3.0 \times 4.5 \text{ mm}^2$. (b) The corresponding 3D rendered structural image (grey color) overlaid with blood flow vascular networks (orange color). The structural image (c) and blood flow image (d) are obtained from a position of proximal nail fold as indicated by the green dashed line. E: epidermis, D: dermis, NM: nail matrix, NR: nail root, NB: nail bed.

3.3 OCT imaging of mouse brain *in vivo*

As brain research is such an attractive field in neuroscience, here we also utilized this scalable wide-field OCT-based angiography system for cerebrovascular imaging of whole brain in mice with skull left intact at one single acquisition. All experimental animal procedures prepared for this pilot study of imaging were reviewed and approved by the Institute of Animal Care and Use Committee (IACUC) of University of Washington (Protocol number: 4262-01).

A three-month-old SKH1-E mouse weighing 23g purchased from Charles River Laboratories was used in the study. Prior to vascular imaging, the animal was anesthetized with 1.5% isoflurane (0.2 L/min O₂, 0.8L/min air). The body temperature was maintained by a heating pad during the entire surgery and imaging process. The scalp was retracted to expose the entire skull of the brain. We added several drops of saline on the skull to maintain the hydration of the skull during imaging procedure. After this simple intact-skull preparation, the animal was immobilized in a custom-made stereotaxic stage. In the imaging protocol, we applied the 5 B-scan repetitions per location with 500 A scans per B-scan and 500 locations. Figure 7(a) gives the 3D rendered image resulting from overlaying the OCT tissue structure and OMAG vascular networks while Fig. 7(b) illustrates the image from the OCT tissue structure alone. The FOV in the imaging setting was $20 \times 20 \text{ mm}^2$ that covers the whole head of the animal in a single scan. The wide-field imaging provides rich morphological and vascular information extending from the eye to the neck at a glance, including the structure and blood vessels of olfactory lobes, cerebrum, cerebellum and pineal gland. The midline of the brain separates the left cerebrum from the right cerebrum. The bregma indicates the position where the coronal suture is intersected perpendicularly by the sagittal suture. Figure 7(c) is the OMAG angiographic image that demonstrates the entire vascular network system in the mouse brain. The yellow arrow points to blood vessels of large size that plays an important role for the supply of oxygen and nutrients to the brain. In Fig. 7(d), we show the OMAG image resulted from by reducing the scanning range to $8.5 \times 8.5 \text{ mm}^2$ of the area indicated by the red dashed box in Fig. 7(c) for better visualization of the main blood vessels of the left hemisphere. The networks and branches of MCA and ACA, which are the major arteries to supply blood to cerebrum, are clearly identified. The rich blood vessels in this region is of great value for the investigation of a number of neurological disorders, e.g. stroke, traumatic brain injury, Alzheimer *etc.*

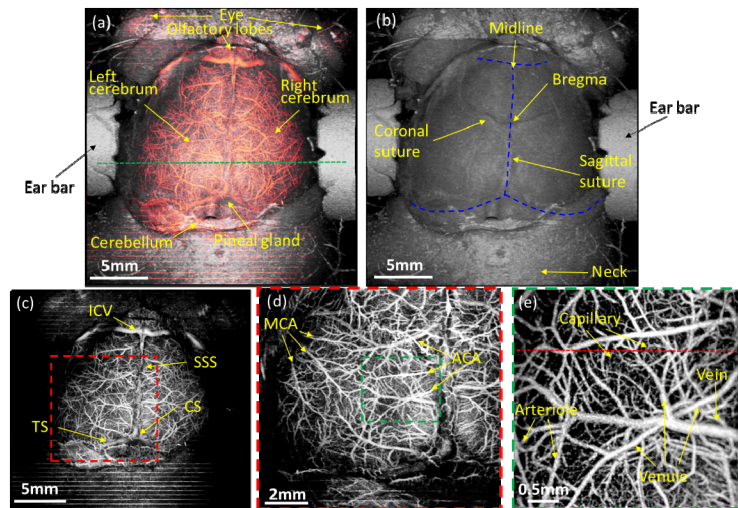


Fig. 7. Wide field imaging provides an opportunity to image whole brain in mouse with just one 3D scan. (a) 3D rendered structural image (grey color) overlaid with vascular networks (orange color) of the whole brain in a mouse with $20 \times 20 \text{ mm}^2$ FOV by using the wide-field imaging mode. Corresponding structural image (b) and *en face* MIP vascular image (c) of the whole brain in mouse, respectively. (d) Zoomed-in *en face* MIP vascular image of the area as indicated in the red dashed box in (c) with $8.5 \times 8.5 \text{ mm}^2$ FOV captured by wide-field mode. (e) The *en face* MIP vascular image for the region of the green dashed box in (d) with $3 \times 3 \text{ mm}^2$ FOV captured by the high-resolution imaging mode. ICV: inferior cerebral vein, SSS: superior sagittal sinus, CS: confluence of sinuses, TS: transverse sinus, MCA: middle cerebral artery, ACA: anterior cerebral artery.

Because the wide FOV imaging mode has a spatial resolution of $\sim 25\ \mu\text{m}$, it is difficult to differentiate capillary details from the image. An ability to visualize functional capillary vessels is often needed in the investigation of brain functions at microscopic scale. To fulfil this requirement, our proposed system has the option to switch the wide FOV to high-resolution FOV mode. In Fig. 7(e), we provide a representative result that was obtained from by setting the FOV at $3 \times 3\ \text{mm}^2$ using high-resolution scanning mode, where the detailed blood vessels of different size such as veins, venules, arterioles and even capillaries are readily identified with the skull left intact. The yellow arrows with annotations point to the representative blood vessels. The ability of vascular visualization at capillary-level ($<10\ \mu\text{m}$) would enable the monitoring of microvascular changes in microcirculation system, which could serve as an important indicator for disease diagnosis, wound healing and drug treatment.

Figures 8(a) and 8(b) provide representative cross-sectional wide-field structural and corresponding vascular images of the mouse brain at the location indicated by the green dashed line in Fig. 7(a). In the wide-field imaging mode, our OCT-based angiography system has a good penetration power that enables the visualization of deep-layer tissue compartments in the mouse brain with skull left intact. This ability is largely attributed to the relatively long ranging distance of 7.5 mm with a sensitivity roll-off of $\sim 0.23\ \text{mm/dB}$ for the system, in addition to the use of 1,310 nm light source. In Fig. 8(a), the boundary between the hard tissue of the skull layer and soft tissue of the cortex is well distinguished due to the highly scattering effect. Between the tissue of cortex and hippocampus, there are also multiple structural layers such as corpus callosum, alveus of hippocampus and stratum oriens that can be identified. In the mouse brain, the highly vascularized central nervous system is enclosed by a layer called meninges that consists of dura matter, arachnoid matter and pia matter [23]. As shown in Fig. 8(b), the dashed yellow line indicates the boundary between the cortex and meninges. The majority of the blood vessels are distributed at the top within the cortex, while there are still some blood vessels located within the meninges that can be identified as indicated by the red arrows in Fig. 8(b), even though the spatial resolution is relatively low in the wide FOV imaging mode.

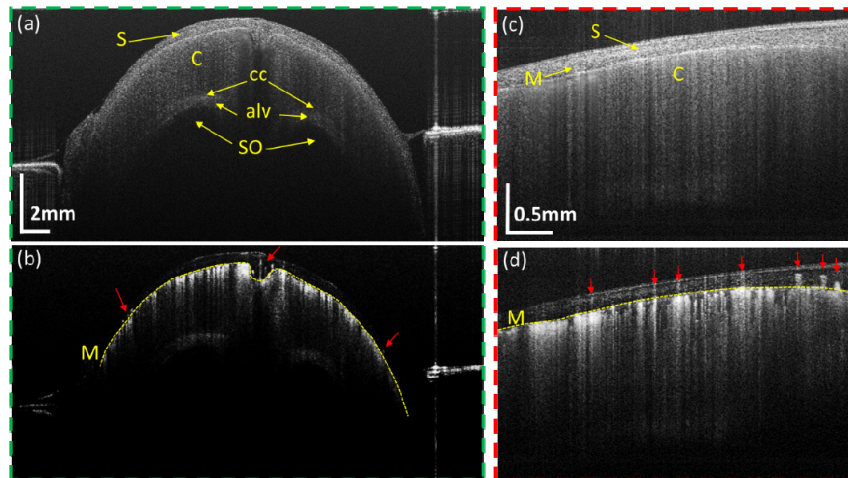


Fig. 8. Proposed system is capable of providing detailed anatomical features of both structure and vascular information in mouse brain. (a) Representative B-scan structural image and (b) the corresponding blood flow image of the mouse brain at the position indicated by the green dashed line in Fig. 7(a) using wide-field mode. (c) and (d) are the same as that of (a) and (b), but from high-resolution FOV mode, captured from a position indicated by the red dashed line in Fig. 7(e). The red arrows point to the blood vessels in meninges. S: skull, C: cortex, cc: corpus callosum, alv: alveus of hippocampus, SO: stratum oriens, M: meninges.

Figures 8(c) and 8(d) illustrate representative cross-sectional structural and corresponding vascular images of the mouse brain at the location indicated by the red dashed line in Fig. 7(e) captured by the high-resolution mode of the OCT system. In this high-resolution mode, the layer of meninges can be clearly seen, which separates the skull from the cortical tissue. The blood flow from relatively big arterioles and venules to capillaries can be differentiated. The blood vessels within the meninges (red arrows) are also identified at the position above the yellow dashed line. The functional scalable images from the wide-field vascular map to capillary-level microcirculation within the cortex and meninges is thus useful for improving our understanding of the neurovascular systems. Due to the light scattering and photon propagation within the functional blood vessels, there is projection artifact of elongated shape of blood vessels in the cerebral tissue, which is sometimes known as “projection artifact”. This artifact may affect the interpretation of the results because it distorts the shape of blood vessels or leads to “false” blood flow signals at places where it is known to be avascular. Zhang *et al* has recently proposed a method that can effectively eliminate this projection artifacts in the OCT-based angiography in retinal imaging [37], which should be explored in the OCT imaging of cerebral blood perfusion in neuroscience in order to improve the interpretation of cerebral vascular images.

4. Discussion and conclusion

In this study, we demonstrated an unprecedented field of view up to 750 mm² for vascular imaging at one single 3D acquisition. This one-time measurement overcomes the drawbacks of most OCT imaging with mosaicking strategy for wide FOV imaging. In many clinical practice, the method of mosaicking for a large FOV requires realignment or refixation of the patient, which is often time consuming, not desirable for clinical translation where the patient compliance is an important issue to consider. Post-processing is also complicated in order to correct distortion, remove overlapping and stitch the mosaic cubes. Thus, to provide an ability of wide-field imaging of both the structural and vascular information would be a very useful addition to the current family of the rapid developments of OCT systems and applications.

In our demonstration of wide FOV imaging, the total size of data set would be inevitably increased compared to the conventional small FOV OCT imaging. In our experiments, the data size ranges from 1,250,000 A-scans to 4,000,000 A-scans, which required ~6 to 30 s to acquire the necessary data sets. While this measurement time may be acceptable for pre-clinical applications, the clinical translation would require even shorter imaging time in order to increase the patient compliance for imaging in humans. With the recent rapid developments of multi-megahertz OCT systems [9, 38, 39], it is optimistic that the acquisition time for wide-field vascular imaging can be reduced to less than one second, which would meet the requirements for clinical translation to most human applications. These high-speed light source techniques could also benefit other functional wide-field OCT such as Doppler OCT for the quantification of blood flow in tissue. In addition, the field of view that we have demonstrated in this study was up to 750 mm², this is mainly limited by the capability of imaging speed that can be afforded by the InGaAs camera used for the demonstration. If a multi-megahertz swept laser source is employed in the system, then even larger field of view should be easily expected with appropriate engineering design of the scanning system.

Moreover, we have demonstrated two imaging modes (wide-field mode and high-resolution mode) using switchable turret that houses desired objective lenses in the OCT-based angiography system. Although only two imaging modes were demonstrated in this study, the switchable turret design can house more than two objective lenses. Thus, it is highly feasible to implement multiple imaging modes with highly scalable field of view and flexible lateral resolution in the vascular imaging for a variety of biomedical applications. Besides, employing a motorized zoom lens with proper system design, would provide continuous zoom function, which is more attractive for scalable FOV OMAG imaging. In our OCT system, it is clear that different imaging mode introduces slightly different image

distortion due to the optics and galvo scanning. This distortion can be corrected through post-image processing or image calibration in system. In this study, we have visualized the scalable wide-field vascular networks in human fingers and mouse brain, demonstrating the practical uses in dermatology and neuroscience. This scalable wide-field OCT-based angiography system is therefore promising to expand its applications in ophthalmology, cardiology and oncology. With quantitative analysis of the blood flow perfusion, blood vessel diameter and blood vessel density, it may be used to aid disease diagnosis and treatment monitoring in clinical applications.

In conclusion, we have implemented a high-sensitive spectral-domain OCT-based angiography system for scalable wide-field vascular imaging. Due to the superior performance of line scan InGaAs camera with 147 klps line rate and 2048 pixel-array, we are able to achieve high-speed data acquisition with enhanced imaging depth. The engineering design in our system enables dual imaging modes, i.e. wide-field mode and high-resolution mode, for scalable field of view with flexible lateral resolution. Using the OMAG scanning protocol with Eigen-decomposition algorithm, we are able to create high-contrast images that can visualize blood vessel networks at a different size scale ranging from big arteries and veins to capillaries. We have demonstrated this scalable wide-field OCT-based angiography for the imaging of vascular networks in human fingers and mouse brain, promising its potential applications in dermatology and neuroscience. It should be highlighted that the ultra-wide field of view (up to 750 mm²) achieved in our system is, to the best of our knowledge, the largest vascular imaging for biological tissue without mosaicking. This scalable wide-field OCT-based angiography system is expected to benefit a wide range of clinical applications.

Acknowledgments

This work was partially supported by grant from the National Heart, Lung, and Blood Institute (R01 HL093140) and National Institute of Biomedical Imaging and Bioengineering (R01 EB009682). The content is solely the responsibility of the authors and does not necessarily represent the official views of grant giving bodies.